Proceedings of the ASME 2010 3rd Joint US-European Fluids Engineering Summer Meeting and
8th International Conference on Nanochannels, Microchannels, and Minichannels
FEDSM-ICNMM2010
August 1-5, 2010, Montreal, Canada

FEDSM-ICNMM2010-' %&- &

MIXING LAYER GROWTH RESPONSE
TO INFLOW FORCING WITH RANDOM PHASE SHIFT

Jordan Ko

Laboratoire de Probabilités
et Modèles Aléatoires,
Université Paris VII,
2 place Jussieu,
75251 Paris Cedex 05, France
Email: jordan.ko@mac.com

Didier Lucor

Institut Jean Le Rond D'Alembert,
UMR UPMC/CNRS 7190,
Université Pierre et Marie Curie,
4 place Jussieu,
75252 Paris Cedex 05, France

Josselin Garnier

Laboratoire de Probabilités
et Modèles Aléatoires,
Université Paris VII,
2 place Jussieu,
75251 Paris Cedex 05, France

ABSTRACT

We study the sensitivity of the formation and the evolution of large-scale coherent structures in spatially developing plane mixing layers to uncertainties in the inflow forcing phase shifts. Instead of examining the mixing layer growth at discrete phase values, a complete response is determined by treating the phase shift as periodic and uniformly distributed random variables. The Fourier Chaos expansion (FCE) is used to decompose the stochastic solution in the abstract random space and the coefficients are determined by the discrete Fourier transformation (DFT). The statistical moments and quantiles of pertinent physical measures were determined. In the bimodal perturbation case, the vortex interactions are sensitive to only a small range of phase differences where large downstream variations in mixing layer growths are observed. In the tri–modal perturbation case, mixing layer growth is especially sensitive to the phase difference between the fundamental and the subharmonic modes immediately downstream from the inlet. Near the downstream location with subharmonic vortices roll up, an increase of the influence of the phase difference between the subharmonic modes can be observed. In both cases, the stochastic phase differences between the perturbation modes are delayed further downstream in comparison to the stochastic perturbation magnitudes. Quantiles of discrete vortex pairing events and different mixing layer length scales are also estimated.

1 Introduction

Mixing layers are found at the interface of two parallel co-flowing streams with different velocities where vortices form due to the Kelvin-Holmholtz instability. Such coherent structure is the hallmark of a spatially developing mixing layer and its subsequent evolution exhibit strong two-dimensional behaviors [1, 2]. The repeated pairing of the vortices leads to the growth of the mixing layer and such a phenomena is dominated by the presence of the subharmonic modes [2].

The formation of coherent structures and the evolution of streamwise vortices are extremely sensitive to flow conditions [3, 4]. Any uncertainties in the geometry, the boundary conditions and the fluid properties can lead to discrepancies when different experimental and numerical studies are compared. Without additional statistical information, the calibration of numerical models against experimental data may lead to erroneous conclusions.

In the numerical simulations, perturbations are needed at the inflow to trigger the formation of streamwise vortices. Such inflow perturbations can be designed based on phase difference, forcing magnitude, and forcing frequency and they often consist of the summation of temporally oscillatory disturbances added on top of the mean flow. Using the linear stability theory (LST), Michalke determined the fundamental perturbation frequency of a mixing layer with a hyperbolic tangent mean velocity pro-

file [5,6].

The effects of the perturbation magnitudes, phase frequencies and phase differences on the mixing layer growth have been the subject of previous studies. The fundamental frequency was shown to obtain the maximum mixing layer growth rate both numerically [7] and experimentally [8]. The effect of the perturbation amplitudes is studied experimentally [8, 9] and numerically [10,11]. It is reported that a larger forcing magnitude causes the energy associated with the subharmonic frequency to grow faster in the streamwise direction, thus triggering the onset of vortex interaction further upstream towards the inlet.

The effect of different *discrete* phase differences is studied numerically [10–19] and experimentally [15, 20]. The phase difference primarily affects the energy transfer between the modes. In the bimodal case, the phase lag leads to a shift in the vortex arrangement in the streamwise direction. The possible vortex interactions range from vortex merging, when the modes are in phase, to vortex shredding, when the phase difference is $\pi/2$ [17].

The knowledge of the system response at a limited number of discrete points may be satisfactory when there is only one uncertain variable (ie. in bimodal perturbation cases). However, a systematic approach which considers the entire parametric space is needed for more complex cases (ie. in trimodal perturbation cases). Moreover, we seek an efficient representation that would account for the inherent uncertainties associated with the forcing parameters. Such uncertainty quantification (UQ) studies have recently received much attention, among others [21–24]. Instead of the Monte Carlo (MC) method, cf. [24], we seek a more efficient approaches such as the generalized Polynomial Chaos (gPC) method [25], which spectrally represents the solution response to system uncertainties and accurately provides the statistical information at a fraction of the cost of the MC methods.

This study will examine the sensitivity of the mixing layer to the uncertainties present in the phase differences between perturbation modes at the inlet with the FCE method. In particular, the sensitivity of the time–averaged vorticity, vorticity thickness and momentum thickness will be examined.

2 Spatially Developing Mixing Layer with random disturbances

Following the formulation by Monkewitz and Huerre [7], the time-averaged streamwise inlet velocity profiles of a 2D mixing layer is defined as

$$\overline{u}_{\text{in}}(y) = 1 + \lambda \tanh(y/2), \qquad (1)$$

where $\lambda = \triangle U/2\overline{U}$ is a measure of the magnitude of the velocity difference and y is the cross-stream coordinate. The mean velocity, $\overline{U}$, and the velocity difference, $\triangle U$, are calculated from the upper and lower streams' velocities. Downstream from the
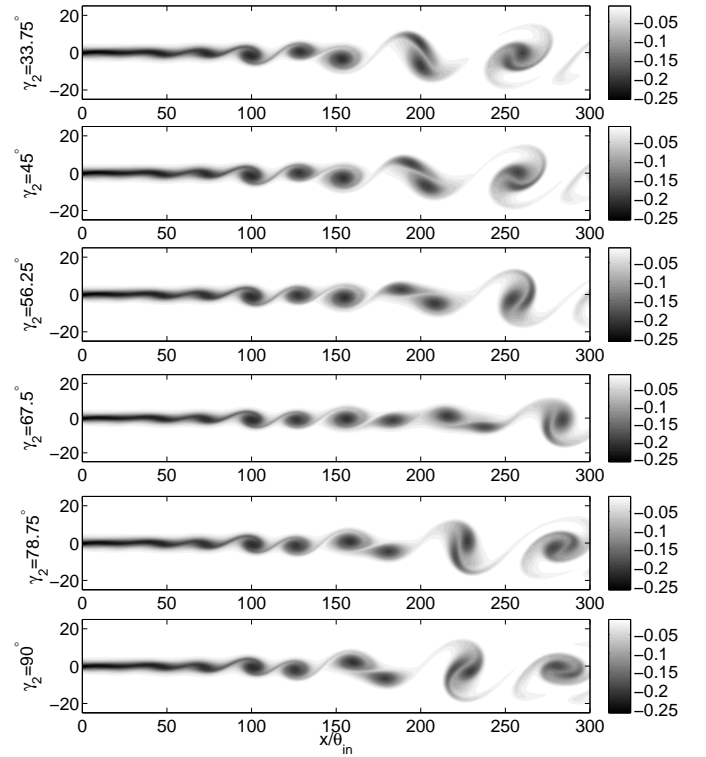

FIGURE 1. DNS instantaneous distributions of vorticity in the 2D mixing layer with bimodal perturbation forcings at different phase differences, γ_2. R=100.

inlet, the spatial growth of the mixing layer is quantified by the vorticity thickness, δ_ω, or momentum thickness, θ. In this study, the Reynolds number is defined using $\overline{U}$ and θ at the inlet. The time-dependent inflow velocity profile is defined as

$$u_{\text{in}}(y,t) = \overline{u}_{\text{in}}(y) + \sum_{n=1}^{N} \varepsilon_n \left[f(y) \sin(\omega_n t + \gamma_n) \right], \qquad (2)$$

where N is the total number of perturbation modes, ε_i the magnitude of each forcing mode and γ_i the phase difference between the i-th and the $(i+1)$-th modes. The variation in the phase difference has a non-trivial effect on the vortex interactions. Several Direct Numerical Simulations (DNS) bi–modal perturbation simulations are presented here to illustrate this influence (cf. Fig. 1) and one can clearly observe that the change in the phase difference leads to visibly different downstream evolutions of the large vortex structures. Here and in the remaining part of the study, the Reynolds number is taken to be $Re = 100$.

In the present study, γ_i are treated as independent and iden-

tically distributed (iid) random variables with finite support, i.e. $\gamma_n = \overline{\gamma_n} + \sigma \xi_n$, where $\xi = \{\xi_n\}_{n=1}^N$ are iid random variables with *uniform* distributions and σ^2 measures the variance of the distribution. In this study, $\overline{\gamma_i}$ is 0 and σ is π.

In the following section, the numerical method used to obtain the stochastic solution and its statistical measures are presented.

3 Numerical Method

The Fourier-chaos approach is used to analyze the system response in the random space and the modal coefficient in the expansion is solved using a collocation method. We consider the complete probability space $(\Omega, \mathscr{F}, \mathscr{P})$ with probability measure $\mathscr{P}$. We call the random event, ω, where $\omega \in \Omega$. Let $\xi = (\xi_1(\omega), ..., \xi_N(\omega))$ be a $\mathbb{R}^N$-valued random variable mapping $(\Omega, \mathscr{F}) \to (\mathbb{R}^N, \mathscr{B}^N)$ where $\mathscr{B}^N$ is the Borel α-algebra on the reals; N is the number of random dimensions. Each random variable lives in the range space $\Gamma_n = \xi_n(\Omega)$ and the total support Γ is $\Gamma = \prod_{n=1}^N \Gamma_n \subset \mathbb{R}^N$. The random field (e.g. velocity field u) is written as a truncated expansion of Fourier chaos basis functions and can be expressed as,

$$u(\mathbf{x}; \xi) = \sum_{k=0}^K \hat{u}(k, \mathbf{x}) \prod_{n=1}^N e^{ik_n \xi_n}, \qquad (3)$$

where the Fourier basis is expressed in term of the Euler's form of the wave number $k_n \in \mathbb{Z}$ and ξ. The number of terms in the expansion is a function of N and the maximum wave number K. In contrast to the finite support used in [26], such basis of expansion admits a periodic support of $\Omega \in [-\pi, \pi]$ and forms an orthonormal basis with respect to the measure, $\rho(\xi) d\xi = \left(\frac{1}{2\pi}\right)^N d\xi$, ie.

$$\langle e^{ij\xi}, e^{ik\xi} \rangle = \left(\frac{1}{2\pi}\right)^N \int_\Gamma e^{ij\xi} \overline{e^{ik\xi}} d\xi = \delta_{jk}. \qquad (4)$$

To determine complex modal coefficients $\hat{u}_k(\mathbf{x})$, we take the inner product of $u(\mathbf{x}; \xi)$ with the Fourier basis. Taking advantage of the orthogonality, we obtain for the one-dimensional case

$$\hat{u}(k, \mathbf{x}) = \left\langle u(\mathbf{x}; \xi), e^{-ik\xi} \right\rangle, \quad \text{for k = 0 ... K.} \qquad (5)$$

Thus, the FCE coefficients in Eq. (3) can be readily determined from Eq. (5) using the discrete Fourier transform (DFT) on equally-spaced quadrature points $\{z_m\}$ on Γ, ie. $\hat{u}(\mathbf{x}; k) = \mathscr{F}(u(\mathbf{x}; z_m))$. The complex coefficients $\hat{u}(k, \mathbf{x})$ contain the amplitude and the phase information of the discrete sinusoidal components in the abstract random space. For higher random dimensions, the DFT can be repeatedly applied to $u(\mathbf{x}; \xi)$ to compute

the integration for $\hat{u}(k, \mathbf{x})$. According to the Nyquist sample theorem, DFT is exact for wavenumbers up to $K = \lfloor \frac{L}{2} - 1 \rfloor$ where L is the number of quadrature points in each dimension and the total number of quadrature points is $N_q = L^N$ for a full-tensor quadrature.

The convergence of such method has not been formally established and we will show that spectral convergence does apply for the Fourier chaos and the statistical measures converges in the L^2 sense when the number of terms is infinite.

Within the framework of the PCM method, the stochastic moments are easily obtained. The mean and variance are

$$\mathbb{E}_\xi[u](\mathbf{x}) = \hat{u}_0(\mathbf{x}) \qquad (6)$$

$$\text{Var}[u(\mathbf{x}; \xi)] = \sum_{k=1}^{N_q} w_k \{u(\mathbf{x}; z_k) - \mathbb{E}[u(\mathbf{x}; \xi)]\}^2. \qquad (7)$$

Skewness and kurtosis of the solution can also be similarly determined. Additionally the Sobol' sensitivity index [27] can be used to identify the influence of each random parameter. One can also easily construct response surfaces from the explicit form of the FCE representation (cf. Eq. (3)). The response surface is very useful as it provides a graphic illustration of the dependance of a physical quantity to the random inputs, that can be related to its PDF.

The quantile of the momentum thickness, $\theta(x; \xi)$, is the value where the probability of $\theta(x; \xi)$ is lower than a prescribed level. We assume that $\theta(x; \xi)$ has a continuous cumulative distribution function (CDF), $F(\theta_\alpha(x)) = \mathbb{P}(\theta(x; \xi) \leq \theta_\alpha(x))$, and the goal is to estimate the α–quantile $\theta_\alpha(x)$ such that $\mathbb{P}(\theta(x; \xi) \leq u\theta_\alpha(x)) = \alpha$. With Monte–Carlo method, $\theta_\alpha(x)$ is estimated by

$$F(\theta_\alpha(x)) = \frac{1}{Z} \sum_{k=1}^Z \mathbf{1}_{\theta(x; \zeta_k) \leq \theta_\alpha} \qquad (8)$$

where ζ_k are independent random variables generated according to the distributions of $\xi(\omega)$. The total number of Monte Carlo samples, Z, needs to be large to accurately estimate extreme quantiles where α is very large or small.

With complex numerical models, it can be prohibitive to evaluate a large number of samples and the estimated quantile may be inaccurate. Instead of evaluating the numerical model directly, it is preferable to evaluate Eq. (3) from which a large number of samples can be computed relatively cheaply. Since the FCE representation of $\theta(\mathbf{x}; \xi)$ is more accurate near the origin of the random space, it may fail in regions where $\theta(x; \xi_\alpha) = \theta_\alpha$. Thus, refinements with local generalized polynomial chaos (gPC) representations near ξ_α are used to improve the accuracy of the quantile estimation.
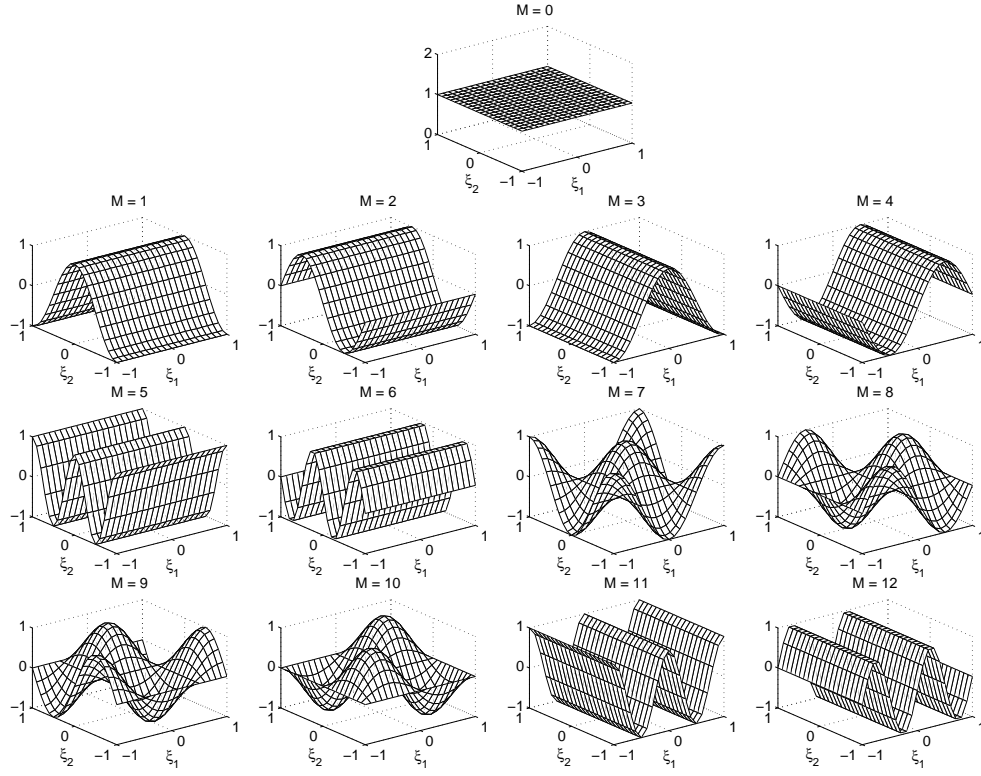
FIGURE 2. The Fourier basis of expansion for $N = 2$ up to $K = 2$. The first row contains the constant term in the Fourier basis. The second row contains the Fourier basis terms with a wave number of $\sum k_n = 1$. The third and fourth rows contain the Fourier basis terms with a wave number of $\sum k_n = 2$.

The refinement points, ξ_α, are located using the Lagrange multiplier method. In the current case, the limit state function is

$$G(x;\xi) = \sum_{k=0}^{K} \hat{\theta}(k,x) \prod_{n=1}^{N} e^{ik_n\xi_n} - \theta_\alpha(x) = 0 \qquad (9)$$

and the objective function is clearly the distance of ξ to the mean of the random variable, μ. By searching for the point on Eq. (9) with the minimum distance to the origin, we locate the most probable point on the hypersurface.

Combining the original element, Ω, and the refinements in non–overlapping elements D_β, the decomposition of the random space is

$$D = \begin{cases} D_{\text{gPC}} = \Omega \setminus D_\beta, \\ D_\beta = \cup D_k, \\ D_i \cap D_j = \emptyset & \text{if } i \neq j, \end{cases} \qquad (10)$$

where D_k is the support of each refined element. By combin-

ing different FCE and gPC representations of $u(\mathbf{x};\xi)$ in D, we obtained the following meta–model for the estimation u_α:

$$u(\mathbf{x};\xi) = \begin{cases} \sum_{k=0}^{K} \hat{u}(k,\mathbf{x}) \prod_{n=1}^{N} e^{ik_n\xi_n} & \text{if } \xi \in D_{\text{gPC}}, \\ \sum_{m=0}^{M} \hat{u}_m^*(\mathbf{x}) \theta_m(\varphi) & \text{if } \xi \in D_k, \end{cases} \qquad (11)$$

where $\hat{u}_m^*$ are the gPC coefficients, φ the random variable having the support D_k and the $\theta_m(\varphi)$ the canonical orthogonal polynomial basis chosen based on the probability density function (PDF) of φ.

The deterministic solutions are computed using a DNS 2D incompressible Navier-Stokes equations solver, $\mathcal{N}\varepsilon\kappa\mathcal{T}\alpha r$ [28]. The validations of the DNS solver and the FCE method will be shown.

4 Validation

A non-intrusive stochastic spectral projection method is used to study the effect of stochastic phase differences on the

growth of plane mixing layer where the stochastic outputs are represented using the Fourier Chaos expansion. This approach involves multi-dimensional numerical integration of the solution over the random domain and the collocation points are evaluated using DNS solvers of the Naviers-Stokes equations. Robustness and accuracy of the obtained statistical results should be reliable as both deterministic and stochastic numerical methods used are fully spectral.

4.1 DNS Solver

The DNS solver $\mathcal{N}\varepsilon\kappa\mathcal{T}\alpha r$ utilizes hierarchical spectral/hp expansions on hybrid subdomains. In the current study, quadrilateral elements are used over the entire flow domain and they are populated with Jacobi polynomial nodes corresponding to high order 2D mixed weights. The order of the polynomials, P_J, can be spatially adjusted to provide spectral refinement but a constant P_J is used in this study. A minimum Jacobi polynomial order $P_J=12$ in each mesh cell is found to be sufficient for all cases. The non–linear products are handled effectively by a collocation approach followed by a Galerkin projection. A stiffly-stable pressure correction-type scheme is employed with a second-order accuracy in time for the temporal integration [29].

A Dirichlet time-dependent velocity boundary condition with periodic perturbations is used at the inlet. The streamwise velocity profile is defined by Eq. (2). For the validation case treated below, cross-stream velocity perturbation is added. The entire flow domain is initialized with the hyperbolic tangent mean flow without perturbations. Neumann boundary condition is used on the three remaining boundaries. A reasonable grid aspect ratio is used due to the cross-stream growth the mixing layer in the streamwise direction, following recommendation of Wilson and Demuren [30]. The domain sizes and the mesh resolution are listed in Table 1. The mesh parameters provide a sufficiently fine mesh resolution for a uniform grid [30, 31].

TABLE 1. Geometry and mesh resolution for the DNS realization needed for the bi–modal and tri–modal perturbation cases.

	Height	Length	Grid cells
bi–modal	$120\,\theta_{in}$	$360\,\theta_{in}$	24×36 quad. elements
tri–modal	$240\,\theta_{in}$	$600\,\theta_{in}$	48×60 quad. elements

The Navier-Stokes equations are non-dimensionalized with $\bar{U}$ and θ_{in}. The mean and variance chosen for the ε_i are such that the range of variability of each magnitude is in the $[0, 10\%\bar{U}]$ interval. This range of perturbation magnitude will be used in this study unless stated otherwise. The wavenumbers n_i are chosen to best match the LST profiles. That explains why the cross-stream scale is not doubled when the streamwise scale doubles for each subharmonic. The corresponding non-dimensional wavelengths

are 5, 6.667 and 10 respectively, when normalized with θ_{in}. One can see that the effects of the perturbation decay to 10%, 1% and 0.1% of $\bar{U}$ at cross-stream positions of 2.94, 5.29 and 7.60 θ_{in}.

The validation of the DNS solver is performed against the 2D DNS results from Wilson and Demuren [30]. Different mesh refinements and P values were tested for the bi– and tri–modal perturbation cases and the final configuration is listed in Table 1. The deterministic inflow parameters for the bi–modal case are listed in Table 2. The DNS solver captures well the vortical structure and the momentum thickness growth of the mixing layer when compared to the results in [30]. For details of the validation, readers are referred to [32].

TABLE 2. Validation case: inflow parameters from the Wilson and Demuren study [30].

Re	λ	$\varepsilon_{1,2}$	ω_1	ω_2
100	0.538	$2.12\%\bar{U}$	0.22	0.11

Each simulation is run for at least twelve periods of the lowest perturbation mode and flow statistics are collected over the last four periods of the run. This is enough for the time-averaged flow quantities to converge and the transient effects due to the initial conditions to be convected out.

4.2 Quadrature Convergence

The ability of Newton-Cotes grid to obtain accurate quadrature approximation the solution response in random space is tested here. The L^2-norm of the PCM variance error from the bi–modal perturbation case is determined at different downstream positions by using the PCM variance with highest quadrature level as a pseudo-exact values, cf. Fig. 3. Overall, spectral convergences are observed. As the degree of non–linear interaction increases further downstream, the quadrature level required to achieve the same level of accuracy increases correspondingly.

4.3 Fourier Chaos Convergence

The accuracy of the FC approximation of the stochastic variable can be examined by its K-convergence where K is the wavenumber of the Fourier series. The FC variances for increasing K is computed and the L^2-norm error is determined with respect to the PCM variance. As increasingly higher terms in the Fourier series are included in the expansion, the magnitude of the truncation should decrease and the FC variance should converged towards the PCM variance. Indeed for the one-dimensional case, good convergence is observed and continuous K-convergence is observed at all downstream positions, cf. Fig. 4. As the degree of non-linear vortex interaction increases further downstream, the K

TABLE 3. Numerical parameters for the bi–modal and tri–modal perturbation cases. The wavelength, ω_3, and wave number, n_3, are only used for the tri–modal perturbation case.

Re	λ	$\overline{\varepsilon_i}$	σ_i	ω_1	ω_2	ω_3	n_1	n_2	n_3
100	0.5	$5\%\overline{U}$	$5\%\overline{U}$	0.22	0.11	0.073	0.4π	0.3π	0.2π
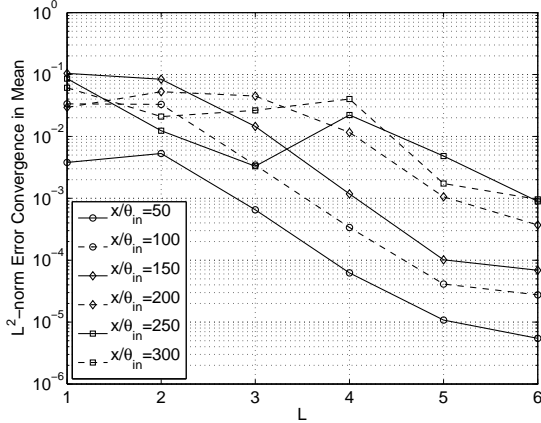
FIGURE 3. The convergence in the PCM mean with increasing quadrature levels in the bimodal perturbation, i.e. $N = 1$, case.

required to obtain a target accuracy also increases. However, the two dimensional case, the convergence rate is smaller.

TABLE 4. Numerical parameters for the bi–modal and tri–modal perturbation cases. The second subharmonic frequency, ω_3, is used only in the tri-modal case.

Re	λ	$\overline{\varepsilon_i}$	σ_i	ω_1	ω_2	ω_3	$\overline{\gamma_i}$	σ
100	0.5	$5\%\overline{U}$	$5\%\overline{U}$	0.22	0.11	0.073	0	π

FIGURE 4. The convergence in the FCE variance with terms having increasing wavenumber, K: (a) the bimodal perturbation case, i.e. $N = 1$, and (b) the trimodal perturbation case, i.e. $N = 2$.

5 Results

In this section, the results of the forced plane mixing layer subject to bi–modal and tri–modal perturbations are presented and discussed. The perturbation parameters are listed in Table 4. The stochastic collocation procedure for the bi–modal and tri–modal case employed quadrature levels of L=64 and L=9 (i.e. N_q=64 and N_q=81 points) and FC expansions with K=30 and K=8, respectively. K is the wave number of the sinusoidal functions.

5.1 Sensitivity Analysis

The sequential amalgamation of successive vortices in a mixing layer is the primary mechanism of the mixing layer growth. The
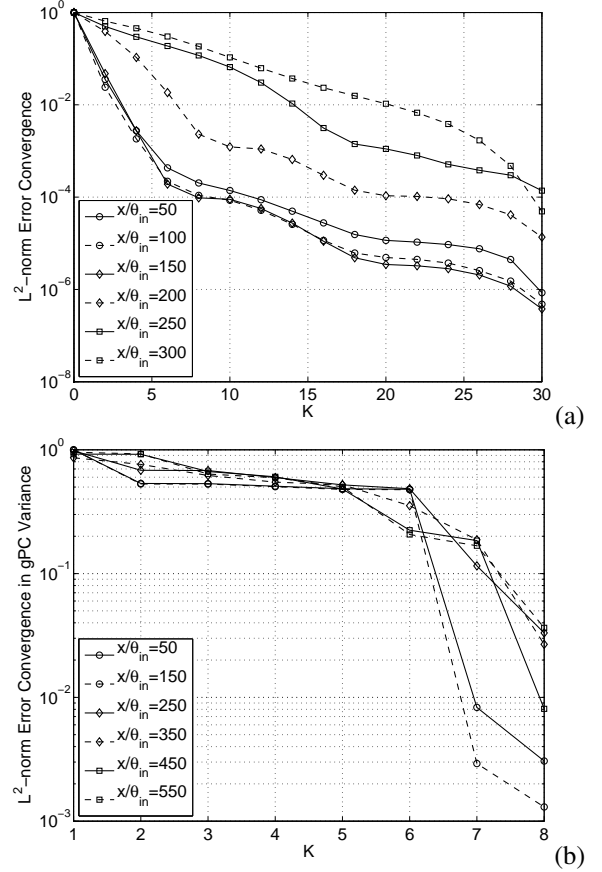
phase differences, γ_i, alters the timing and location of these interactions, leading to different growth rates. Hence, the uncertainty in the phase difference would have a significant effect in regions where the vortices interact. It can be observed in Fig. 1 that vortex roll-ups all take place between x/θ_{in}=125 and x/θ_{in}=200 for the various phase differences shown.

The mean and variance of the time-averaged vorticity of a bimodal perturbation case where the phase difference varies uniformly in the support $[-\pi, \pi]$ is shown in Fig. 5. One can observe that the mean contour remains mostly unchanged from the inlet up to x/θ_{in}=125, where the fundamental vortex pairing starts to occur. After this point the mean contour gradually spreads
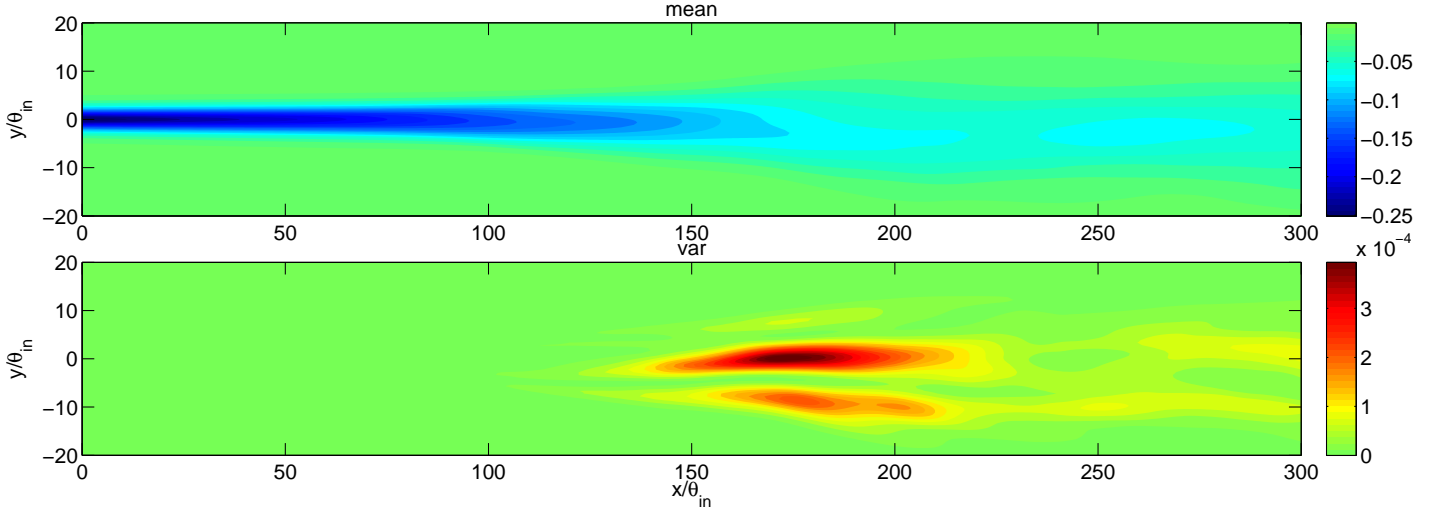
FIGURE 5. Spatial distributions of the mean and variance of the time-averaged vorticity in the mixing layer with bi–modal perturbation forcing.

out in the cross-stream direction until about x/θ_{in}=250. In this zone where vortex pairing takes place, the variance has its largest value. In comparison with the variance contour from the stochastic perturbation magnitude study where the contour magnitude is large between x/θ_{in}=100 and x/θ_{in}=200, the phase different vorticity variance contour lags in the streamwise direction and is more compact.

The contours of the stochastic mean and variance of the time-averaged vorticity from the tri–modal perturbation case are shown in Fig. 6. From the deterministic results, the growth of the mixing layer can be observed to take place in two successive distinct stages (i.e. from x/θ_{in}=100 to x/θ_{in}=200 and from x/θ_{in}=250 to x/θ_{in}=450). These two zones are associated respectively with the vortex pairing events of the fundamental and the subharmonic modes. In the zone where the fundamental vortex pairing occurs, a variance contour similar to that of the bimodal case is observed in the fundamental vortex pairing zone. Its magnitude is comparable to that of the bimodal case. Further downstream, the phase difference between the subharmonic modes does not appear to have significant influence in the zone where the secondary vortex-roll up. The large variance in the zone associated with the fundamental vortex roll-up suggests that the uncertainties in the phase differences have significant affect on the initial vortex pairing between the fundamental and the subharmonic modes. In contrast, the second phase difference affects mostly the sequence of vortex pairing associated with the second subharmonic mode but the timing of the pairing remains relatively unchanged, cf. [11]. Thus the variance contour downstream of x/θ_{in}=250 is almost negligible.

The streamwise growth of the mixing layer can be quantified by the momentum and the vorticity thicknesses. As successive vortex pairing events occur, the thickness measures in-

crease in step-wise fashion with increasing x. The effect of the stochastic phase differences can thus be observed in the variance of the downstream thickness measures. The streamwise evolutions of the vorticity and momentum thicknesses are shown in Fig. 7 and 8.

In the bimodal case, the growths of the momentum and the vorticity thicknesses are slow immediately downstream of the inlet. During vortex roll-up and pairing, the thickness measures start to increase more rapidly. Since the vorticity thickness, δ_ω, is a cross-stream differential measure, it is less smooth compared to the momentum thickness, θ, which is a cross-tream integral measure. In the zone where the vortex pairing takes place, increases in the variances of δ_ω and θ are observed. However, upon the completion of the vortex pairing process, the variances in the solutions due to the stochastic phase difference remain large. This is in stark contrast with the stochastic perturbation magnitude case where the variance immediately decreases after vortex pairing is complete. The downstream evolutions of δ_ω and θ for the trimodal case are shown Fig. 8. The growth reaches $\delta_\omega/\delta_{\omega,in}$=4.0 at x/θ_{in}=200 after the first vortex pairing sequence. The second plateau at about $\delta_\omega/\delta_{\omega,in}$=8 does not occur until x/θ_{in}=200, well after the second vortex rollup. The growth of the variance profiles in both thickness measures are also continuous. In both the bimodal and the trimodal case, it is observed that the variances θ increased visibly more upstream than δ_ω. This is an indication that, although the variation in the phase difference is most significant during vortex pairing, its influence can already be detected in the vortex roll-up zone.

The phase difference affects the mixing layer growth in the bi–modal perturbation cases primarily through altering the vortex interaction patterns. It has been confirmed both experimentally by Ho & Huang (1981) and numerically by Inoue (1991) that the
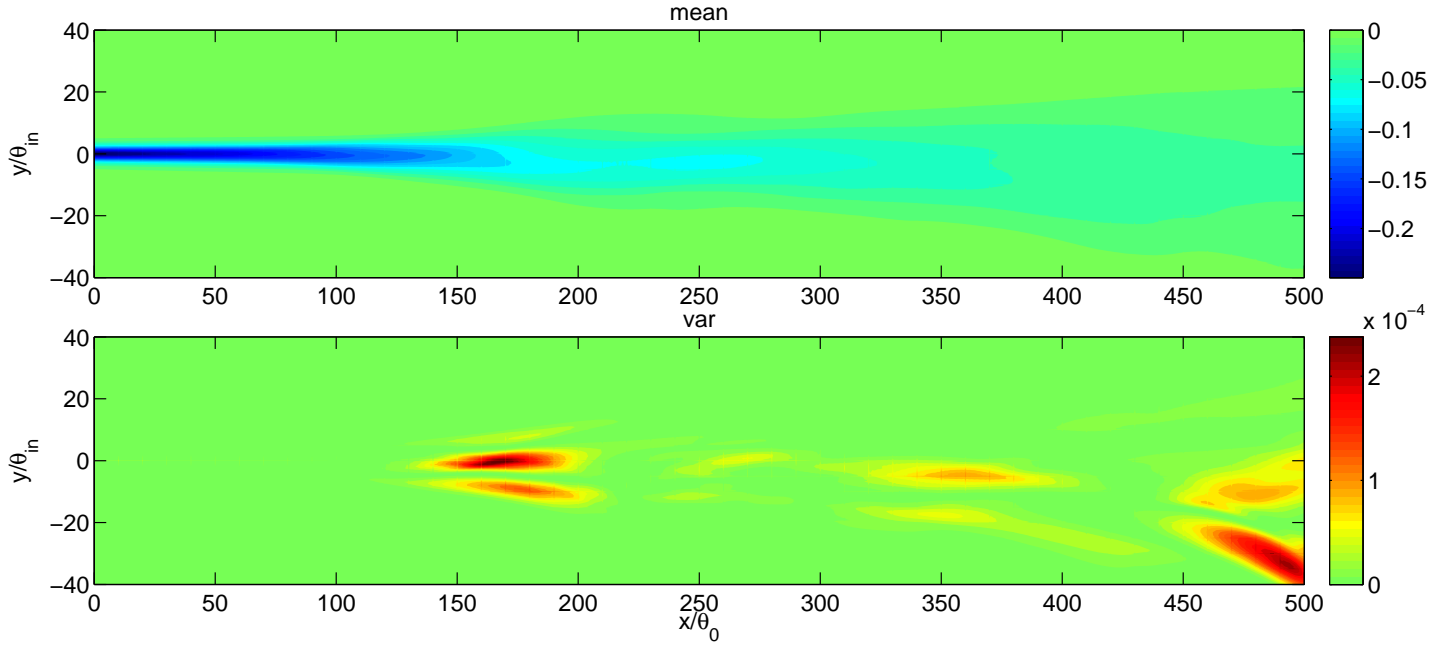
7

FIGURE 6. Spatial distributions of the mean and variance of the time-averaged vorticity in the mixing layer with tri–modal perturbation forcing.
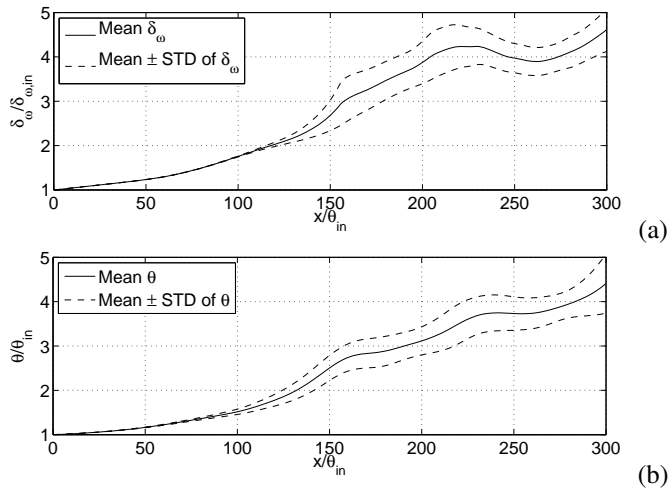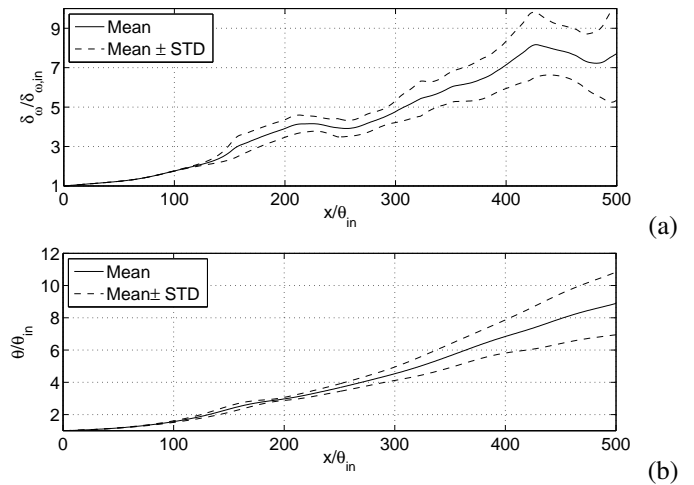

FIGURE 7. Streamwise distributions of the mean solution and standard deviation envelop of (a) $\delta_\omega/\delta_{\omega,in}$ and (b) θ/θ_{in} for the mixing layer with bi–modal perturbation forcing.

FIGURE 8. Streamwise distributions of the mean solution and standard deviation envelop of (a) $\delta_\omega/\delta_{\omega,in}$ and (b) θ/θ_{in} for the mixing layer with tri–modal perturbation forcing.

vortex formation localizes when the phase difference is near $\pi/2$. The localization of vortex formation implies that the streamwise growths of the energy associated with the fundamental and the subharmonic components are synchronized, leading to a faster growth in the mixing layer. In contrast, sharp drop in the mixing layer growth was observed when the phase difference approaches 0. Furthermore, the subharmonic component of the mixing layer growth was the more significantly affected.

5.2 Response Variability
Using the explicit form of the FC representation, cf. Eq. (3), it is straightforward to build response surfaces of any output quantity of the system. For the bimodal case, the solutions over the support $[-\pi, \pi]$ can be plotted using a polar diagram, where the
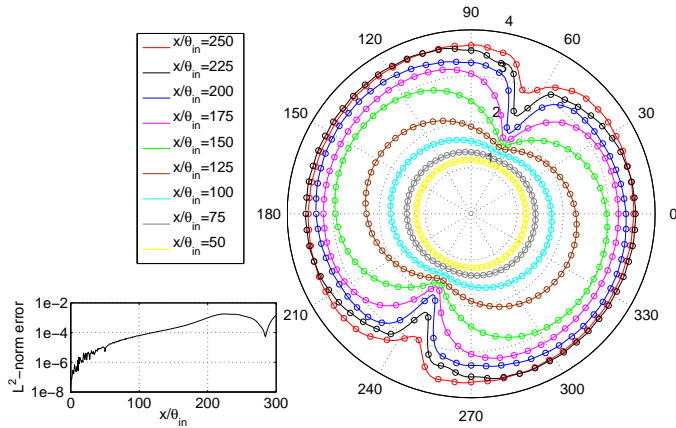
FIGURE 9. Response curves of $\theta/\theta_{\mathrm{in}}$ vs. γ_2 for the bimodal perturbation forcing at different streamwise positions and the streamwise L^2-norm error of the reconstructed θ.

radius represent the thickness measures and the angle represents the phase difference γ_1. The circle formed by the solutions will gradually expand outwards from the origin. If the phase difference has no influence on the mixing layer growth, the circle will grow in a concentric manner with increasing x. In contrast, any hindrance or enhancement of the mixing layer growth will be readily revealed as an ellipse in the polar diagram.

It has been observed both experimentally [15] and numerically [10] that the vortex formation is localized when the phase difference is near $90°$. The localization of vortex formation implies that the streamwise growths of the energy associated with the fundamental and the subharmonic components are synchronized, leading to a faster growth in the mixing layer. In contrast, sharp drop in the mixing layer growth was observed when the phase difference approaches $0°$ with the subharmonic component of the mixing layer growth being the more affected. Consequently, one would expect to observe an ellipse with a major axis along $\gamma = 90°$ and the minor axis along $\gamma = 0°$.

The $\theta/\theta_{\mathrm{in}}$ response for the bimodal case are generated using 360 samples *uniformly* distributed over the parametric domain, Γ, and are displayed in polar diagrams in Fig. 9. Before the vortex pairing occurs, the phase difference has no influence on the mixing layer growth. Thus θ profiles appear to be circular at x/θ_{in}=100. As the vortex pairing commences near x/θ_{in}=125, elliptical shapes in the thickness profiles start to developed with the major axis pointing in the phase difference angles which trigger the mixing layer growth first. At x/θ_{in}=150, ellipses with the major axis along γ_1=150° and γ_1=330° are observed. The enhanced mixing layer growths at these two phase differences continue, as visible in the enlarged ellipses at x/θ_{in}=200. Further downstream, the vortex interaction eventually commences for mixing layer with other phase difference values. At x/θ_{in}=250,
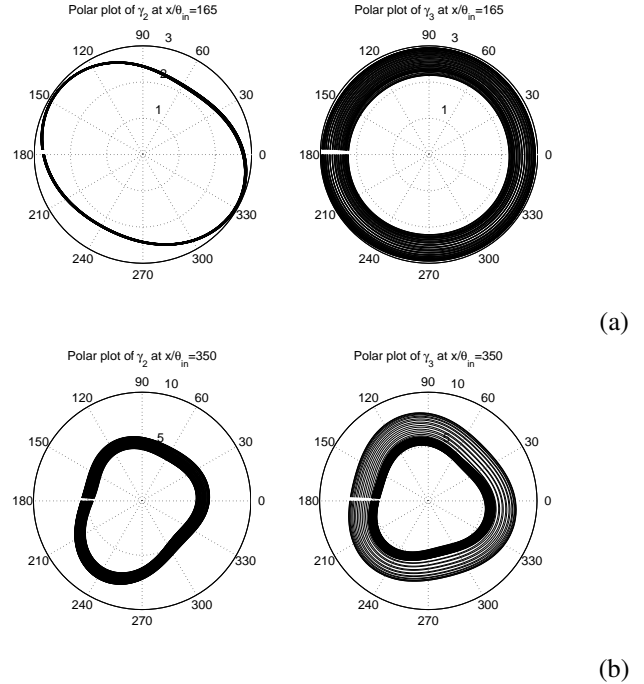

(a)

(b)

FIGURE 10. The polar plots of θ at different values of phase shift. The polar plots of γ_2 vs. θ at different γ_3 values are shown on the left and those of γ_3 vs. θ at different γ_2 values are on the right. (a) $x/\theta_{in} = 165$. (b) $x/\theta_{in} = 350$.

the delayed mixing layer growths lead to large phase-wise variation in the thickness growth. Such irregularity in the growth is especially evident between $\gamma_1 = 30°$ and $90°$ and its symmetric counterpart between $\gamma_1 = 210°$ and $270°$. The dominance of the mixing layer growth away from γ_1=90 contradicts previous observations [10, 15, 17]. This could be attributed to the fact that arbitrary sinusoidal perturbation profiles were used at the inlet instead of the perturbation profile derived from the linear stability theory.

The $\delta_\omega/\delta_{\omega,in}$ and $\theta/\theta_{\mathrm{in}}$ response surfaces are generated using 40,000 samples *uniformly* distributed over the square parametric domain, Γ. Instead of visualizing the solution responses over the support $[-\pi, \pi]^2$ with three–dimensional spheres, they are plotted as surfaces instead (cf. Fig. 10). Only the evolution of θ is shown here but the analysis is applicable to both thickness measures. The evolution of the thickness measures can be divided into three distinct stages. In the initial stage, the thickness measures vary significantly with changes in γ_1 but not γ_2. This can be observed in the response surfaces at x/θ_{in}=50 and x/θ_{in}=100. In both cases, the response surfaces exhibit large variations in the γ_1-direction but remain unchanged in the γ_2-direction. Further downstream, the variation in γ_2 becomes more dominate as the subharmonic vortex interactions commence. For x/θ_{in}=200, the two phase differences appear to be affecting
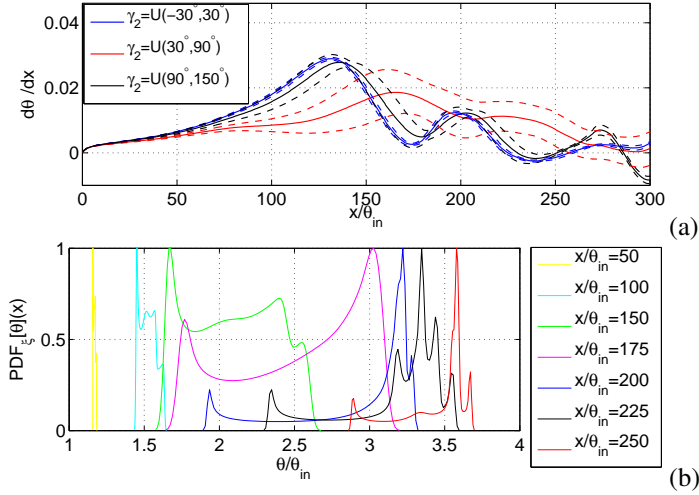
FIGURE 11. (a) Means and standard deviation envelopes of $d\theta(x)/dx$ at three different ranges in γ_2 where γ_2 is assumed to be an uniformly distributed random variable. (b) PDF determined from the uniform distribution $\gamma_2 = U(30°, 90°)$. One million samples are used in all cases.

equally the θ growth. However, at x/θ_{in}=250 and x/θ_{in}=350, one observes larger variation in the thickness measures in the γ_2-direction than the γ_1-direction.

5.3 Different Input Supports

Statistical moments over a smaller support have more physical meaning. The symmetric halves of $\theta(\mathbf{x}, \xi)$ in the bimodal case are divided into three equal parts where γ_2 are assigned a random uniform distribution. The statistical moments are then calculated from one million samples. Since Eq. (3) involves only algebraic evaluations whose L^2–norm error is well below 10^{-2} at all downstream locations for bimodal forcing, such large number of accurate evaluation is possible. The rate of mixing layer growth can be determined from the the streamwise derivative of $\theta(x)$, ie. $d\theta(x)/dx$, and a negative $d\theta(x)/dx$ means that energy is being extracted from the vortical structure to the mean flow. The means and standard deviation envelopes of $d\theta(x)/dx$ for $\gamma_2 = U(330°, 30°)$, $U(30°, 90°)$ and $U(90°, 150°)$ are shown in Fig. 11(a). Earlier and faster mixing layer growths are clearly observed in the first and the third range of γ_2 examined. However, the larger $d\theta(x)/dx$ value also leads to an earlier stagnation of the mixing layer growths. Indeed $U(30°, 90°)$ shows the largest variance in comparison with the other two intervals whose mean and the standard deviations envelopes have similar values. To examined the distribution of the solution, the PDFs of $\theta(\mathbf{x}, \xi)$ are computed by taking an histogram of the one million uniformly distributed samples from Eq. (3). The kernel–smoothing density estimate is used to produce smoother distribu-
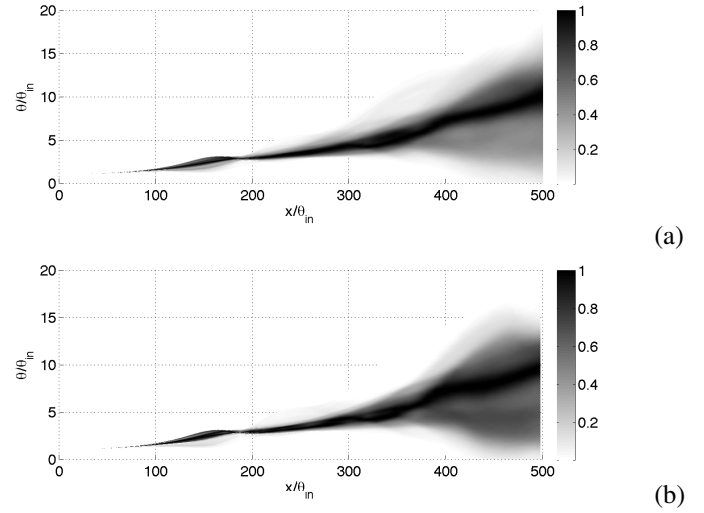

FIGURE 12. Normalized PDF of θ with (a) uniform distribution and (b) beta distribution centered at $\mu = (0, \pi)$ with $\alpha = 10$ and $\beta = 10$.

tions [33]. Initial PDF distributions near the inlet ares narrow, cf. Fig. 11(b). At higher x/θ_{in} where bifurcation in θ occurs, multiple local peaks are observed. In addition, there are also long tails in the PDF distributions suggesting that the a wide range of probable θ values could be present if the phase shift is not precisely controlled in the experiments.

5.4 Quantile Estimation

The PDF of θ are examined in the trimodal case and the FCE with a quadrature level $L = 9$ and $K = 8$ are used. A total of 1×10^5 Monte Carlo samples are used to estimate the PDF at different downstream locations and the PDF profiles are computed using the kernel smoothing function in Matlab. In the first case tested, the random variable is uniformly distributed in D, cf. Fig. 12.(a). The PDF profiles shown are normalized with their respective local maximums to better juxtapose the profile shapes from different downstream locations.

It is unlikely that the phase difference in an experiment could have such a uniform support. Therefore, in the second case, the random variable is assumed to have a beta distribution with $\alpha = \beta = 10$ centered at $\mu = (0, \pi)$, cf. Fig. 12.(b). Such a distribution gives a Gaussian like random variable in a bounded support. The two PDF profiles from the two different random variables are similar because the beta random variable has a variance that is relatively large compare to the domain, ie. $\sigma = 0.472$. Consequently, the beta random variable reproduces smaller parts of the periodic response of $\theta(x, \xi)$ on D.

Next, we estimate the 99%–quantile of θ at $x/\theta_{in} = 400$ where the input is the same beta distribution with $\alpha = \beta = 10$ centered at $\mu = (0, \pi)$. The 99%–quantile of θ is estimated to be $\theta_{99\%} = 9.746$ from 1×10^5 Monte Carlo samples. Using the
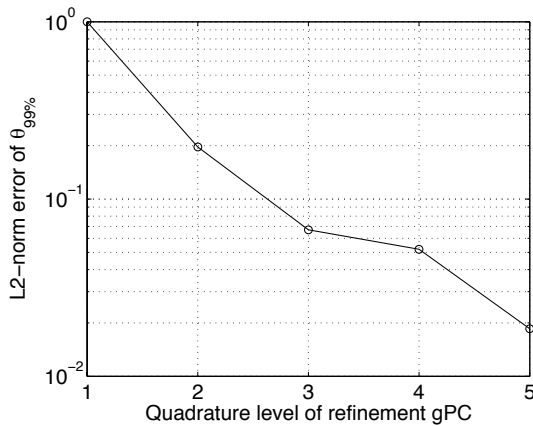
FIGURE 13. The convergence of the L^2–norm error, with increasing L, in the 99%–quantile of $\theta(x, \xi)$ at $x/\theta_{in} = 400$.

Lagrange multiplier method, several local design points, satisfying Eq. (9), were identified. The three design points closest to μ are $\xi_\alpha = (0.196, 2.100)$, $(-1.526, -2.650)$ and $(-1.669 1.779)$ whose $\|\xi\|$ are respectively 1.059, 1.603 and 1.669. Local gPC refinement is centered at $\xi_\alpha = (0.196, 2.100)$ and has a length of 0.472 in both dimensions. Thus, φ has a bounded support and the gPC representation is constructed using the Legendre polynomial. The full–tensor quadrature is used in the refinement zone and the multi-element approach in Eq. (11) is used to compute the 99%–quantile.

Points from quadrature levels $L = 1$ to 6 are evaluated and the local gPC representation is computed. The L^2–norm error of the 99%–quantile is computed using the results from $L = 6$ as the psedu–exact value. The convergence of the errors is shown in Fig. 13. At $L = 6$, an additional 79 samples are required and this is not even sufficient to increase the global collocation level from $K = 9$ to $K = 10$. In contrast, by concentrating the limited computing resource in the region near θ_α, the estimated quantile can be significantly improved.

6 Conclusion

The sensitivity of the vortex interactions in mixing layers to uncertainties in the phase differences in bimodal and trimodal perturbations is studied with the Fourier chaos (FC) expansion. In both the bimodal and the trimodal case, the stochastic phase differences cause variations in the vortex interactions further downstream in comparison to the stochastic perturbation magnitude case. In the bimodal case, the response surfaces of the momentum and vorticity thicknesses show that the thickness growths are spatially steady and phase–wise smooth in a certain range of the phase difference but spatially discontinuous and phase–wise irregular in another well-defined range. In the trimodal case with two perturbation phase differences, vortex interaction dependence on variation of the phase difference between the fundamental and the subharmonic is observed near the inlet followed by regions where the phase difference between the subharmonics leads to distinct peaks. Overall, large oscillation in the thickness growths are observed in the phase difference space. This study also demonstrated that the accuracy of extreme quantile of random outputs can be improved by refining the representation near the location of the quantiles.

REFERENCES

[1] Brown, G. L., and Roshko, A., 1974. "On density effects and large structure in turbulence mixing layer". *Journal of Fluid Mechanics,* **64**, pp. 775–816.

[2] Winant, C. D., and Browand, F. K., 1974. "Vortex pairing: the mechanism of turbulent mixing layer growth at moderate Reynolds number". *Journal of Fluid Mechanics,* **63**, pp. 237–255.

[3] Oster, D., and Wygnanski, I., 1982. "The forced mixing layer between parallel streams". *Journal of Fluid Mechanics,* **123**, pp. 91–130.

[4] G., B. R., 1975. "Some measurements on the effect of tripping the two-dimensional shear layer". *AIAA Paper,* **13**, pp. 245–247.

[5] Michalke, A., 1964. "On the inviscid instability of the hyperbolic-tangent velocity profile". *Journal of Fluid Mechanics,* **19**(4), pp. 543–556.

[6] Michalke, A., 1965. "On spatially growing disturbances in an inviscid shear layer". *Journal of Fluid Mechanics,* **23**(3), pp. 521–544.

[7] Monkewitz, P. A., and Huerre, P., 1982. "Influence of the velocity ratio on the spatial instability of mixing layers". *Physics of Fluids,* **25**(7), July, pp. 1137–1143.

[8] Ho, C.-M., and Huang, L. S., 1982. "Subharmonics and vortex merging in mixing layers". *Journal of Fluid Mechanics,* **119**, pp. 443–473.

[9] Zhou, M. D., and Wygnanski, I., 2001. "The response of a mixing layer formed between parallel streams to a concomitant excitation at two frequencies". *Journal of Fluid Mechanics,* **441**, pp. 139–168.

[10] Inoue, O., 1992. "Double-frequency forcing on spatially growing mixing layers". *Journal of Fluid Mechanics,* **234**, p. 553.

[11] Inoue, O., 1995. "Note on multiple-frequency forcing on

mixing layers". *Fluid Dynamics Research, 16*, pp. 161–172.

[12] Davis, R. W., and Moore, E. F., 1985. "A numerical study of vortex merging in mixing layers". *Physics of Fluids, 28*(6), pp. 1626–1635.

[13] Patnaik, P. C., Sherman, F. S., and Corcos, G. M., 1976. "A numerical simulation of Kelvin-Helmholtz wave of finite amplitude". *Journal of Fluid Mechanics, 73*(2), pp. 215–240.

[14] Corcos, G. M., and Sherman, F. S., 1976. "Vorticity concentration and the dynamics of unstable free shear layers". *Journal of Fluid Mechanics, 74*, p. 241.

[15] Ho, C.-M., and Zhang, Y.-Q., 1981. "On the manipulation of spreading rates of forced mixing layers". In Proceedings of 3rd International Symposium on Turbulent Shear Flows, pp. 75–81.

[16] Comte, P., Lesieur, M., Laroche, H., and Normand, X., 1989. "Numerical simulations of turbulent plane shear layers". In *Turbulent shear flows 6*, J.-C. André, J. Cousteix, F. Durst, B. E. Launder, F. W. Schmidt, and J. H. Whitelaw, eds. Springer-Verlag, Berlin, pp. 361–380.

[17] Riley, J. J., and Metcalfe, R. W., 1980. "Direct numerical simulation of a perturbed, turbulent mixing layer". *AIAA Paper, 80-0274*.

[18] Sandham, N. D., and Reynolds, W. C., 1989. "Some inlet-plane effects on the numerically simulated spatially-developing mixing layer". In *Turbulent shear flows 6*, J.-C. André, J. Cousteix, F. Durst, B. E. Launder, F. W. Schmidt, and J. H. Whitelaw, eds. Springer-Verlag, Berlin, pp. 441–454.

[19] Stanley, S., and Sarkar, S., 1997. "Simulations of spatially developing two-dimensional shear layers and jets". *Theoretical computational fluid dynamics, 9*, pp. 121–147.

[20] Zhang, Y.-Q., Ho, C.-M., and Monkewitz, P., 1984. "The mixing layer forced by fundamental and subharmonic". In IUTAM Symposium, V. V. Kozlov, ed., Springer-Verlag, pp. 385–395.

[21] Hou, T. Y., Luo, W., Rozovskii, B., and Zhou, H.-M., 2006. "Wiener Chaos expansions and numerical solutions of randomly forced equations of fluid mechanics". *Journal of Computational Physics, 216*, pp. 687–706.

[22] Yu, Y., Zhao, M., Lee, T., Pestieau, N., Bo, W., Glimm, J., and Grove, J., 2006. "Uncertainty quantification for chaotic computational fluid dynamics". *Journal of Computational Physics, 217*, pp. 200–216.

[23] Lucor, D., Meyers, J., and Sagaut, P., To appear. "Sensitivity analysis of LES to subgrid-scale-model parametric uncertainty using polynomial chaos". *Journal of Fluid Mechanics*.

[24] Schmid, P. J., 2007. "Nonmodal stability theory". *Annual review of Fluid Mechanics, 39*, pp. 129–162.

[25] Xiu, D., and Karniadakis, G. E., 2002. "The Wiener-Askey polynomial chaos for stochastic differential equations". *SIAM Journal of Scientific Computing, 24*(2), pp. 691–644.

[26] Millman, D. R., King, P. I., and Beran, P. S., 2005. "Airfoil Pitch-and-Plunge Bifurcation Behavior with Fourier Chaos Expansions". *Journal of Aircraft, 42*(2), pp. 376–384.

[27] Sobol', I. M., 1993. "Sensitivity estimate for non-linear mathematical models". *Mathematical modelling and computational experiments, 1*, pp. 407–414.

[28] Karniadakis, G. E., and Sherwin, S. J., 2005. *Spectral/hp Element Methods for CFD*. Oxford University Press, New York.

[29] Karniadakis, G. E., Israeli, M., and Orszag, S. A., 1991. "High-order splitting methods for the impressible Navier-Stokes equations". *Journal of Computational Physics, 97*, pp. 414–443.

[30] Wilson, R. V., and Demuren, A. O., 1994. Numerical simulation of two-dimensional spatially-developing mixing layer. Tech. Rep. NAS1-19480, NASA Langley Research Center.

[31] De Bruin, I., 2001. "Direct and large-eddy simulation of the spatial turbulent mixing layer". PhD thesis, University of Twente, Twente, the Netherlands.

[32] Ko, J., Lucor, D., and Sagaut, P., 2008. "Sensitivity of two-dimensional spatially developing mixing layers with respect to uncertain inflow conditions". *Physics of Fluids, 20*(7), p. 077102.

[33] Wand, M. P., and Jones, M. C., 1995. "Kernel smoothing". In *Monographs on Statistics and Applied Probability*. Chapman and Hall/CRC.